

Ga intercalation in van der Waals layers for advancing p-type Bi_2Te_3-based thermoelectrics

Yiyuan Chen(陈艺源), Qing Shi(石青), Yan Zhong(钟艳), Ruiheng Li(李瑞恒), Liwei Lin(林黎蔚), Ding Ren(任丁), Bo Liu(刘波), and Ran Ang(昂然)

Citation: Chin. Phys. B, 2023, 32 (**6**): 067201. DOI: 10.1088/1674-1056/acc2af
Journal homepage: http://cpb.iphy.ac.cn; http://iopscience.iop.org/cpb

What follows is a list of articles you may be interested in

Advancing thermoelectrics by suppressing deep-level defects in Pb-doped $AgCrSe_2$ alloys

Yadong Wang(王亚东), Fujie Zhang(张富界), Xuri Rao(饶旭日), Haoran Feng(冯皓然), Liwei Lin(林黎蔚), Ding Ren(任丁), Bo Liu(刘波), and Ran Ang(昂然)
Chin. Phys. B, 2023, 32 (**4**): 047202. DOI: 10.1088/1674-1056/acb765

Interface-induced topological phase and doping-modulated bandgap of two-dimensioanl graphene-like networks

Ningjing Yang(杨柠境), Hai Yang(杨海), and Guojun Jin(金国钧)
Chin. Phys. B, 2023, 32 (**1**): 017201. DOI: 10.1088/1674-1056/ac904d

Large Seebeck coefficient resulting from chiral interactions in triangular triple quantum dots

Yi-Ming Liu(刘一铭) and Jian-Hua Wei(魏建华)
Chin. Phys. B, 2022, 31 (**9**): 097201. DOI: 10.1088/1674-1056/ac6dae

Effect of carbon nanotubes addition on thermoelectric properties of $Ca_3Co_4O_9$ ceramics

Ya-Nan Li(李亚男), Ping Wu(吴平), Shi-Ping Zhang(张师平), Yi-Li Pei(裴艺丽), Jin-Guang Yang(杨金光), Sen Chen(陈森), and Li Wang(王立)
Chin. Phys. B, 2022, 31 (**4**): 047203. DOI: 10.1088/1674-1056/ac4bd2

Thermoelectric performance of XI_2 (X = Ge, Sn, Pb) bilayers

Nan Lu(陆楠) and Jie Guan(管杰)
Chin. Phys. B, 2022, 31 (**4**): 047201. DOI: 10.1088/1674-1056/ac474c

---

Ga intercalation in van der Waals layers for advancing p-type Bi_2Te_3-based thermoelectrics

Yiyuan Chen(陈艺源)[1,†], Qing Shi(石青)[1,†], Yan Zhong(钟艳)[1], Ruiheng Li(李瑞恒)[1], Liwei Lin(林黎蔚)[1], Ding Ren(任丁)[1,‡], Bo Liu(刘波)[1], and Ran Ang(昂然)[1,2,§]

[1] *Key Laboratory of Radiation Physics and Technology, Ministry of Education, Institute of Nuclear Science and Technology, Sichuan University, Chengdu* 610064, *China*

[2] *Institute of New Energy and Low-Carbon Technology, Sichuan University, Chengdu* 610065, *China*

(Received 3 December 2022; revised manuscript received 12 February 2023; accepted manuscript online 9 March 2023)

Tetradymite-structured chalcogenides, such as Bi_2Te_3 and Sb_2Te_3, are quasi-two-dimensional (2D) layered compounds, which are significant thermoelectric materials applied near room temperature. The intercalation of guest species in van der Waals (vdW) gap implemented for tunning properties has attracted much attention in recent years. We attempt to insert Ga atoms in the vdW gap between the Te layers in p-type $Bi_{0.3}Sb_{1.7}Te_3$ (BST) for further improving thermoelectrics. The vdW-related defects (including extrinsic interstitial and intrinsic defects) induced by Ga intercalation can not only modulate the carrier concentration but also enhance the texture, thereby yielding excellent electrical properties, which are reflected in the power factor $PF \sim 4.43$ mW·m^{-1}·K^{-2}. Furthermore, the intercalation of Ga produces multi-scale lattice imperfections such as point defects, Te precipitations, and nanopores, realizing the low lattice thermal conductivity in BST-Ga samples. Ultimately, a peak $zT \sim 1.1$ at 373 K is achieved in the BST-1% Ga sample and greatly improved by $\sim 22\%$ compared to the pristine BST. The weak bonding of vdW interlayer interaction can boost the synergistic effect for advancing BST-based or other layered thermoelectrics.

Keywords: thermoelectricity, p-type $(Bi,Sb)_2Te_3$, van der Waals gap defects, texture alignment

PACS: 72.15.Jf, 73.50.Lw, 74.25.fc, 74.25.fg **DOI:** 10.1088/1674-1056/acc2af

1. Introduction

Thermoelectrics as a direct heat-to-electricity conversion technology is one of the most viable energy harvesting candidates, which has been developed in various applications to address the energy crisis and environmental degradation.[1,2] The conversion efficiency of thermoelectric (TE) devices is determined by a dimensionless figure of merit $zT = S^2\sigma T/\kappa_t$, where S is the Seebeck coefficient, σ is the electrical conductivity, T is the absolute temperature, and κ_t $(= \kappa_e + \kappa_L + \kappa_b)$ is the total thermal conductivity, in which κ_e, κ_L, and κ_b are the thermal conductivity of electronic, lattice, and bipolar diffusion, respectively.[3]

The zT, however, is severely limited to ~ 1 because of the complex coupling relationship among these TE parameters. With continuing vigorous development over the past decades, the improvement of power factor ($PF = S^2\sigma$) can be achieved by adjusting the electronic band structure, including tunning the band gap,[4,5] resonance level,[6,7] and band convergence.[8–10] Moreover, the κ_L generally considered as a tunable parameter independently can be reduced by phonon engineering such as nanostructure engineering,[11–13] superionic conductor,[14–16] and defect engineering.[17–19]

The Bi_2Te_3 and its alloys are the best bulk TE materials near room temperature in both n-type and p-type, stacked quai-2D layers, and also are identified as promising topological insulators.[20,21] The crystal structure includes quintuple layers along the c-axis direction, i.e., Bi atomic layer and Te atomic layer alternatively arranged according to Te1–Bi–Te2–Bi–Te1 with a van der Waals (vdW) gap between adjacent Te1:Te1 atoms.[22] This weak interlayer interaction usually involves intrinsic defects, including antisite (AS) defects, vacancies, and vacancies adjunctive defects (e.g., dislocations, misfit defects, and interfaces).[23,24] The abundant dangling bonds between vdW interlayers caused by these defects provide an intriguing platform for achieving high TE properties. Atomic interface design in vdW gap has been devoted to exploring and investigating the effect of microstructure modification on TE properties.[25–28]

Tremendous reports have covered that the atom with a small ionic radius such as Li, Cu, and Ag can be embedded the tetrahedral vacancies in the vdW gap of n-type Bi_2Te_3-based alloys,[29–35] which can not only produce the donor effect to regulate electron carriers but also provide electron transport channels to improve the carrier mobility.[36,37] On the contrary, the intercalation of guest species in p-type Bi_2Te_3-based lattice is not efficient consistently for optimizing TE performance due to the minority carriers produced to impede the carrier concentration in the optimal region. There is no literature reporting

[†]These authors contributed equally to this work.

[‡]Corresponding author. E-mail: rending2k@scu.edu.cn

[§]Corresponding author. E-mail: rang@scu.edu.cn

© 2023 Chinese Physical Society and IOP Publishing Ltd

that intercalation atoms have a positive effect on TE properties of p-type Bi_2Te_3-based alloys to our knowledge.

In this work, we attempt to intercalate Ga into p-type $Bi_{0.3}Sb_{1.7}Te_3$ (BST) lattice to optimize TE performance. The intercalation of Ga produces vdW gap defects, including extrinsic interstitial and intrinsic point defects (i.e., AS defects Bi'_{Te} and Te vacancies), which not only regulates the carrier concentration but also facilitates texture alignment to provide electron transport channels. The increase of weighted mobility μ_W of BST-Ga samples facilitates an excellent *PF* in the whole temperature range. Raman studies and scanning electron microscope images of BST-Ga samples reveal an ultralow κ_L in comparison to the pristine BST because of various types of lattice imperfections including atom-related defects, Te precipitations, and nanopores. As a result, the increased μ_W and decreased κ_L predict the improvement of the quality factor β in BST-Ga samples. Finally, the BST-1%Ga sample achieves a peak $zT \sim 1.1$ at 373 K, obtaining a theoretical conversion efficiency η of $\sim 8.24\%$ in the temperature range of 303 K–500 K.

2. Experimental details

A series of polycrystalline $Bi_{0.3}Sb_{1.7}Te_3$-*x* at% Ga ($x = 0$, 0.5, 1, 1.5) was synthesized by a high-speed swing ball miller (MSK-SFM-3-I) at 1800 rpm for 30 min under an Ar atmosphere, using commercial high-purity elements [Bi, Te, Sb, and Ga (99.99%)]. The milling powders were loaded into a graphite mold and consolidated by hot-pressing method under Ar atmosphere for 15 min at 723 K with a 50 MPa pressure. The densities (ρ) of as-sintered samples were measured by high-precision solid densitometer ($> 98\%$ of theoretical density). The densified samples were cut into disk-like pieces (Φ12.5 mm × 1.5 mm) for the thermal diffusivity measurements, and cuboid pieces along the pressing direction were cut (2 mm × 2 mm × 8 mm) for σ and *S* measurements, respectively. The measurement of electrical and thermal transport parameters was performed along the same direction (parallel to the pressing direction).

X-ray diffraction (XRD) measurements for as-sintered samples along two directions (parallel and perpendicular to the pressing direction) were performed on an x-ray diffractometer with the wavelength of 1.5418 Å (Cu-K_α) to investigate the crystalline phase and grain orientation. The structure refinements were implemented by Rietveld analysis. The microstructure and phase composition were investigated by scanning electron microscope (SEM, JEOL 7100) attached with an energy dispersive spectroscopy (EDS). Room temperature Raman spectroscopic studies were implemented in the frequency range of 30 cm^{-1}–300 cm^{-1} using 633 nm laser excitation with an ultralow frequency filter, 1800 gr/mm grating, and thermoelectric cooled charged coupled device in backscattering configuration. Attenuated total reflection Fourier transformed infrared spectroscopy (ATR-FTIR) of as-sintered samples was compared using Fisher Scientific NICOLET iS 5 (Thermo Fisher Scientific, Waltham, Ma, USA). The IR-reflection spectra were obtained between 4000 cm^{-1} and 400 cm^{-1} after 15 scans.

The Hall mobility and Hall carrier concentration were determined using a Van der Pauw technique under a reversible magnetic field of 1.5 T. The temperature-dependent σ and *S* on the pellets along the two directions were performed using a CTApro instrument (Beijing Cryoall Science and Technology Co., Ltd, China). The thermal conductivity κ was calculated by $\kappa = \rho C_p D$, where ρ is the density, *D* is the thermal diffusivity measured by a laser flash technique (NETZSCH LFA 467), and C_p is the specific heat capacity determined by the Dulong–Petit law.

3. Results and discussion

The XRD patterns of BST-Ga samples parallel to the pressing direction are measured at room temperature, as shown in Fig. 1(a). All the diffraction peaks are consistent with the standard Bi_2Te_3 structure (PDF#49-1713) card without additional impurity peaks, within the detectable limit of XRD. The typical (015) peak gradually shifts to the left with the increase of Ga content, indicating a slight lattice expansion in BST-Ga samples. Lattice constants *c* and *a* are obtained by structural Rietveld refinements, as shown in Fig. 1(b), where the lattice parameter *c* shows the first increasing and then decreasing trend, while the lattice parameter *a* remains almost a constant. Considering the ion radius of Ga^{3+} (0.62 Å) less than that of Bi^{3+} (0.96 Å) or Sb^{3+} (0.76 Å), the variation of lattice parameters can be explained as the insertion of Ga in the vdW gap of BST lattices to increase the distance between the weak vdW force bounded layers rather than substitution, in the case of a minute amount of Ga intercalation ($x < 1.0$). Similar results have also been reported that Cu^+ (0.96 Å) was inserted in the vdW gap of n-type Bi_2Te_3.[32] Contrary to increased lattice constants slightly, a downward trend of lattice parameter for $x = 1.5$ sample can be attributed to the evolution of intrinsic point defects as the number of Ga increases or the formation of Ga-related phase, which both can affect the magnitude of lattice parameters.

The microstructure and composition of BST-Ga samples in cross-section are characterized by SEM with EDS mapping, as shown in Fig. 2. Clearly, a relatively uniform distribution of the constituent elements and the free of impurities in the samples are shown in Fig. 2(e). Nevertheless, the pristine BST is well crystallized with a minute amount of nanopores (Fig. 2(a)), while higher density nanopores (marked with orange arrows) are observed around the surface of BST-*x* at% Ga

samples ($x > 0$), as shown in Figs. 2(b)–2(d). The formation of nanopores may originate from the sublimation of Te segregations during high-temperature solidification because of its high vapor pressure (723 K),[38] compared to other elements with high boiling point such as Sb (1860 K), Bi (2273 K), and Ga (2676 K). This result is consistent with the anomalous effect of Ga intercalation in lattice parameters caused by the intrinsic point defects, especially Te vacancies. Notably, the distribution of nanopores induced by Te precipitates (as a lubricant) sublimating is perpendicular to the pressing direction preferentially,[39] which facilitates the grain orientation of the sintered samples, thereby leading to a more pronounced lamellar structure in SEM cross-sectional images. It should be pointed out that TE properties are analyzed in a direction parallel to the pressing to eliminate the isotropic effect in this work.

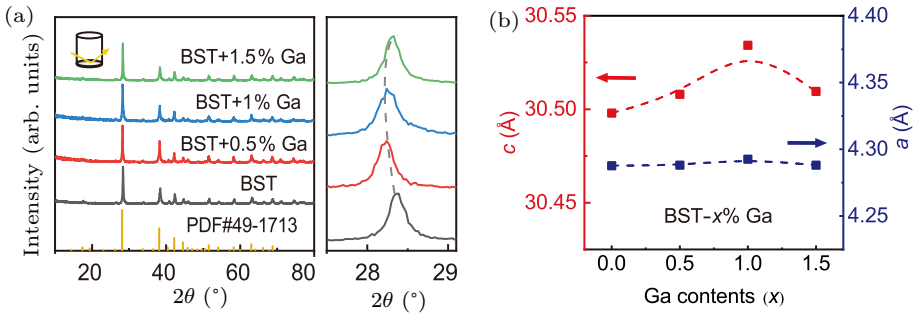


Fig. 1. (a) XRD patterns of as-sintered BST-Ga samples parallel to the pressing direction at room temperature. (b) Lattice parameters as a function of Ga contents x.

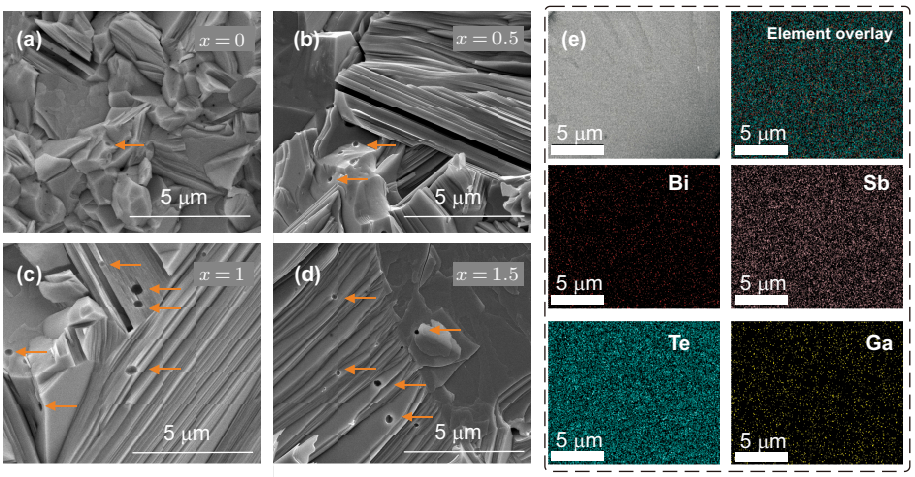


Fig. 2. Room-temperature SEM images for as-sintered BST-Ga samples parallel to the pressing direction. (a) $x = 0$, (b) $x = 0.5$, (c) $x = 1$, (d) $x = 1.5$, and (e) EDS mapping for $x = 1$ samples.

The variation in electrical transport parameters with the amount of Ga intercalation can be understood from the experimentally measured Hall carrier concentration n_H and mobility μ_H at 303 K–500 K. The n_H value demonstrates an abnormal trend of slight increase in BST-Ga samples (Fig. 3(a)), contrary to the intercalation of Ga entering the vdW gap in the form of trivalent ions (donors, carrying on three electrons) to reduce hole carriers. The results can be attributed to the evolution of intrinsic point defects caused by Ga insertion within tetrahedral vacancies surrounded by Te1 atoms. The Ga intercalation promotes the escape of edge atoms (Te1) in the vdW interlayer to leave Te vacancies V''_{Te} and produce Te segregations, which in turn facilitates the formation of AS defects Bi/Sb'_{Te} (carrying on one hole) and cation vacancies $V'''_{Bi/Sb}$ (carrying on three holes) to provide hole carriers.[40] As a result, in the BST-Ga samples, complex mechanisms of regulating the n_H are determined by Ga intercalation and intrinsic point defects simultaneously. The μ_H value conforming to the decreasing trend of $T^{-1.5}$ indicates that the electron-acoustic scattering mechanism is dominant.[41] Nevertheless, the mobility of BST-Ga samples fluctuates slightly, contrary to the general understanding of μ_H decreasing by various defects such as point defects, Te precipitates, and especially nanopores. This can benefit from the additional electron transfer channel provided by Ga insertion within the vdW binding layers of the pristine BST or enhanced texture to compensate for impeding electron transport by diverse imperfections.

To investigate the variation of TE transport characteristics in detail, the S, σ, and PF values for BST-Ga samples are displayed in Figs. 3(b)–3(d), respectively. The S value at room temperature first decreases and then increases, corresponding to the variation trend of the carrier concentration. Moreover,

the peak of S moves obviously to the right at high temperatures, indicating a delay in the onset of bipolar diffusion. In contrast, the magnitude σ increases in BST-Ga samples due to the collective effect of n_H and μ_H, and especially the value of σ for $x = 1$ sample reaches a relatively high level in comparison to other samples. Consequently, the enhanced PF has maximized ~ 4.43 mW·m^{-1}·K^{-2} at 303 K for the sample with $x = 1$ (Fig. 3(d)). Furthermore, the PF values have been improved in the whole temperature range after the intercalation of Ga, which can also be projected in the average power factor (PF_{ave}) and the engineering power factor (PF_{eng}) [Figs. S1(a) and S1(b)]. The PF_{ave} value of the best samples is over 3.4 mW·m^{-1}·K^{-2} in the temperature range of 303 K–500 K, along with the PF_{eng} value reaching 123 W·m^{-1}·K^{-1} at the temperature difference $\Delta T = 195$ K.

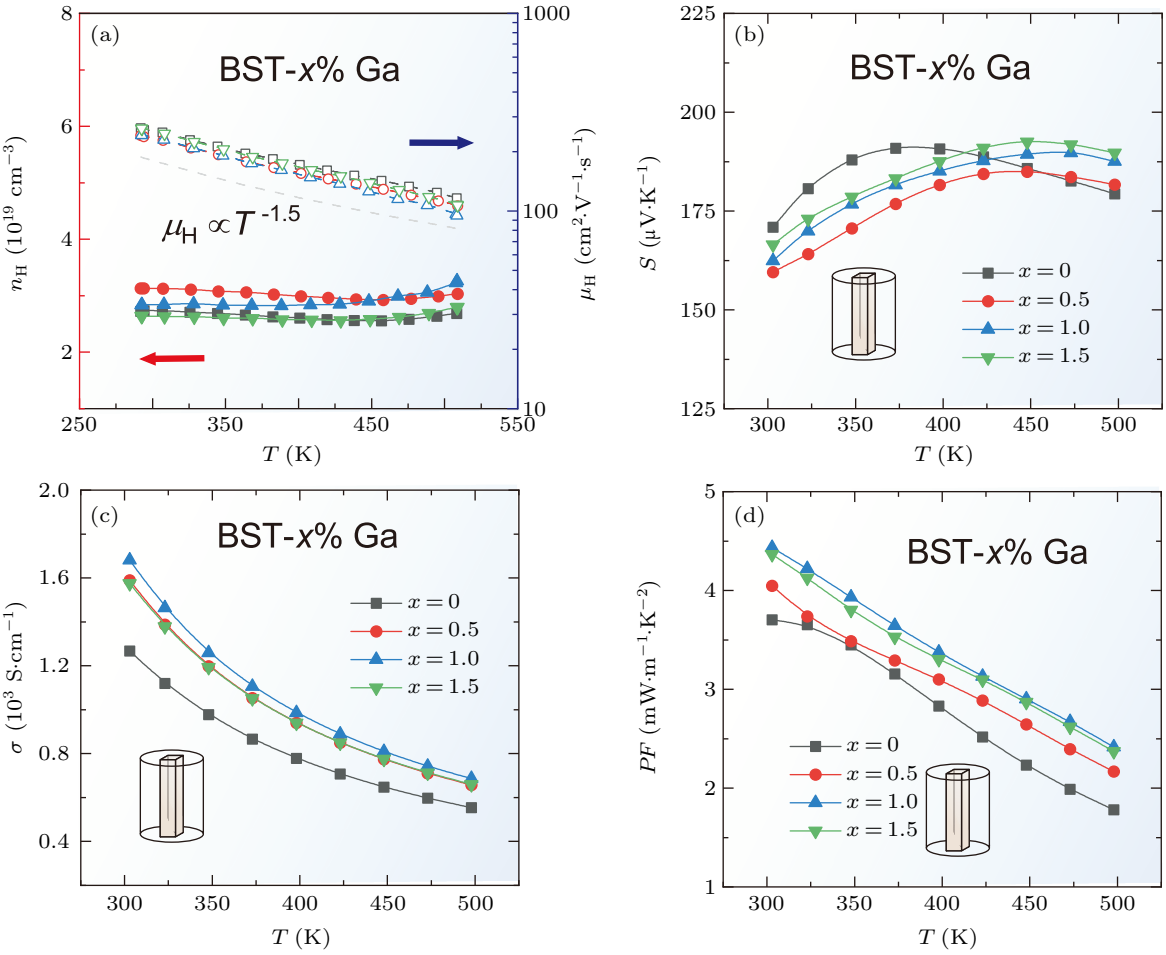


Fig. 3. Temperature-dependent (a) n_H and μ_H, (b) S, (c) σ, and (d) PF for BST-Ga samples.

The density of state (DOS) effective mass m^* and the weighted mobility μ_W can be investigated to further insight into the electrical properties of BST-Ga samples. We estimate m^* value under the assumption of a single parabolic band (SPB) model (see detailed in supporting information), as shown in Fig. 4(a). The S value of all samples falls consistently on the fitted Pisarenko's line, $m^* \sim 0.97m_0$, indicating that Ga intercalation to vdW gaps of BST maintains the density of states at the top of the valence band. Nevertheless, the Ga intercalation can expand the band gap (E_g) of the pristine BST confirmed by the infrared spectroscopy measurements and the Goldsmid–Sharp gap calculations [Fig. S4(b) in supporting information, which is beneficial for single carrier transport to suppress the bipolar diffusion at high temperatures. Enlarging E_g possibly originates from AS defects Bi/Sb$'_{Te}$ induced by Ga intercalation to promote the movement of the first valence band toward near the second valence band.[42] This effect, in turn, can modify individual band degeneracy, which is reflected in μ_W, as shown in Fig. 4(c). The μ_W value increases in the whole temperature range for BST-Ga samples and reaches the maximum value ~ 290 cm^2·V^{-1}·s^{-1} for $x = 1$ sample at 373 K, showing a superior electrical property.

The variation in the composition and microstructure of the pristine BST caused by the intercalation of Ga, not only optimizes the electrical performance but also effectively impedes thermal transport. Figure 5(a) represents the temperature dependence of the total thermal conductivity κ_t and the electronic thermal conductivity κ_e ($= L\sigma T$, Wiedemann–Franz

law, see details in supporting information). At low temperatures, the κ_t values initially decrease with rising temperature due to Umklapp phonon scattering, and then reach their minima and continue to increase. This increasing trend is accounted for the electronic transport process from the intrinsic excitation. The proportion of bipolar conduction and non-electrical contribution from lattice vibration ($\kappa_L + \kappa_b$) are obtained by subtracting κ_e from κ_t, as shown in Fig. 5(b). The value of $\kappa_L + \kappa_b$ (~ 0.47 W·K^{-1}·m^{-1}) for $x = 1$ sample is almost a factor of two lower than that of the pristine BST (~ 0.76 W·K^{-1}·m^{-1}) at 303 K. The decrease of $\kappa_L + \kappa_b$ can be attributed to multi-scale defects induced by the Ga intercalation.

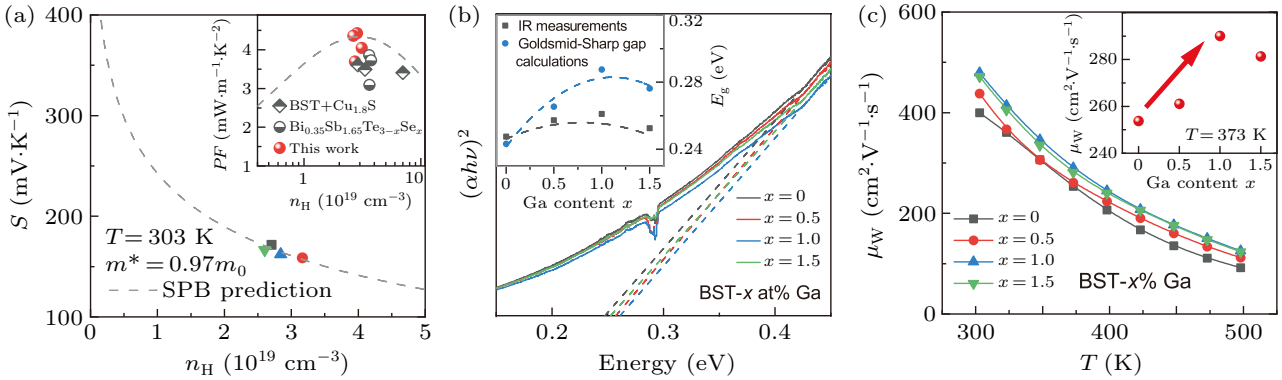


Fig. 4. (a) Room temperature S and PF as a function of n_H for BST-Ga samples. The lines are calculated based on the SPB model and deformation potential theory. Some data from other literatures are selected in the inset as a comparison.[5,19] (b) Infrared spectroscopy band gaps for BST-Ga samples. Inset: measured and calculated band gaps as a function of Ga content x. (c) Temperature-dependent μ_W for BST-Ga samples. Inset: μ_W as a function of Ga content x at 373 K.

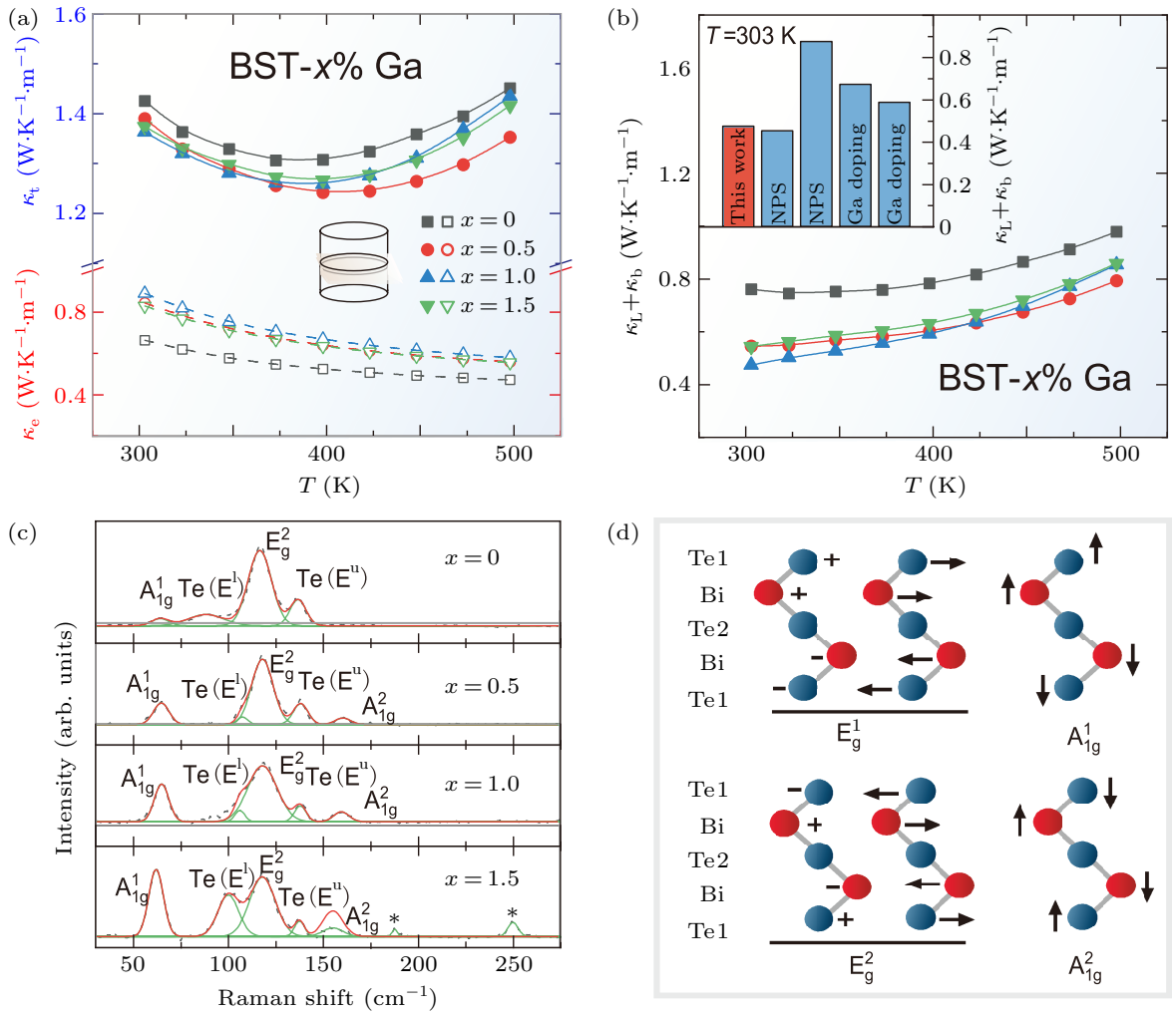


Fig. 5. Temperature dependence of (a) κ_t and κ_e, and (b) $\kappa_L + \kappa_b$ for BST-Ga samples. Inset: compared with the minimum $\kappa_L + \kappa_b$ of other Bi_2Te_3-based materials with nanopores or doped Ga substitutionally.[38,48,50,51] (c) Room temperature Raman spectra of BST-Ga samples. (d) Diagram of the Raman-active vibrational modes.

The inserted Ga atoms form weak bonds with Te1 atoms in the interlayer acting as phonon scattering sites to reduce κ_L. In contrast, the increase of $\kappa_L + \kappa_b$ for $x = 1.5$ sample could be related to forming a more uniform distribution of Ga atoms in the vdW gap, which tends to attenuate phonon scattering.[33] The effect of Ga intercalation on the κ_L can be examined by the variation of the frequency of Raman modes. As shown in Fig. 5(c), the Raman spectrum at room temperature is investigated in the frequency range of 30 cm^{-1}–300 cm^{-1} for BST-Ga samples to identify the effect of intercalation on the lattice vibration. Obviously, there are two main peaks centered at 64 cm^{-1} and 116.5 cm^{-1} in the pristine BST, corresponding to A_{1g}^1 and E_g^2 modes of Sb_2Te_3, respectively.[43] Two low-intensity peaks centered at 88 cm^{-1} and 136.6 cm^{-1} are related to E^l and E^u modes of Te tetrahedra,[44] caused by the segregation of Te atoms during the mechanical or hot-pressing process. The enhancement of peak intensity and the variation of peak position in Raman spectrum indicate the alteration in the atomic arrangement of the pristine BST system with Ga intercalation [Fig. S3(b)]. Notably, the peak of A_{1g}^2 modes centered at $\sim$ 158 cm^{-1} is found in the BST-Ga samples, which can originate from the high-frequency tensile vibration mode activated by Ga intercalation in the vdW gap. Additionally, the appearance of two additional peaks centered at 187.5 cm^{-1} and 249.8 cm^{-1} in the BST-1.5% Ga samples may be assigned to the Ga element or Ga-based compounds.[45,46]

To investigate the effect of nanopores generated by the evaporation of Te precipitations on thermal transport properties, the distribution of nanopore size is statistically analyzed from SEM images. The diameter of nanopores is in the range of 50 nm–800 nm, which is comparable to the medium and long wavelength phonons responsible for the maximum thermal transport to effectively impede phonon thermal transports.[47] Moreover, the number of nanopores can be reflected in the porosity estimated using the following equation:[48]

$$P = (1 - \rho/\rho_0) \times 100\%, \tag{1}$$

where P is the porosity, ρ_0 is the theoretical density of the pristine BST (without nanopores), and ρ is the density of BST-Ga samples. The estimated porosity for BST-Ga samples is listed in Table 1, indicating that the high-density nanopores can effectively impede phonon transport.[49] Compared with other Bi_2Te_3-based materials with nanopores or Ga-doped materials, as shown in the inset of Fig. 5(b), the $\kappa_L + \kappa_b$ value of the best sample in this work shows remarkable competitiveness.[38,48,50,51]

The dimensionless figure of merit zT is achieved by considering the effect of various defects produced by Ga intercalation into the BST lattice on the electrical and thermal transport parameters. As shown in Fig. 6(a), the peak zT for $x = 1$ sample reaches $\sim$ 1.1 at 373 K. And also, the average zT (zT_{ave}) and the TE conversion efficiency η for BST-Ga samples in the temperature range of 303 K–500 K are displayed in Fig. 6(b), and the η value for $x = 1$ sample reaches $\sim$ 8.24% in the whole temperature region. To further get insight into the origin of enhanced zT, the quality factor β ($\propto \mu_W/\kappa_L$) ranging from $\sim$ 0.1 to $\sim$ 0.8 at 373 K is calculated (see details in supporting information), as shown in Fig. 6(c). The β value for $x = 1$ sample reaches $\sim$ 0.6, a 36% improvement over the pristine BST ($\sim$ 0.38), which is superior competitive compared to other Bi_2Te_3-based materials.[38,48,50,51] The increase of β, as discussed above, can be attributed to synergistic effects of increased μ_W and decreased κ_L.

Table 1. The measured density and estimated porosity of BST-Ga samples.

Samples	Measured density (g·cm^{-1})	Porosity (%)
Pristine	6.685	0.22
Ga-0.5%	6.633	0.99
Ga-1%	6.557	2.14
Ga-1.5%	6.596	1.56

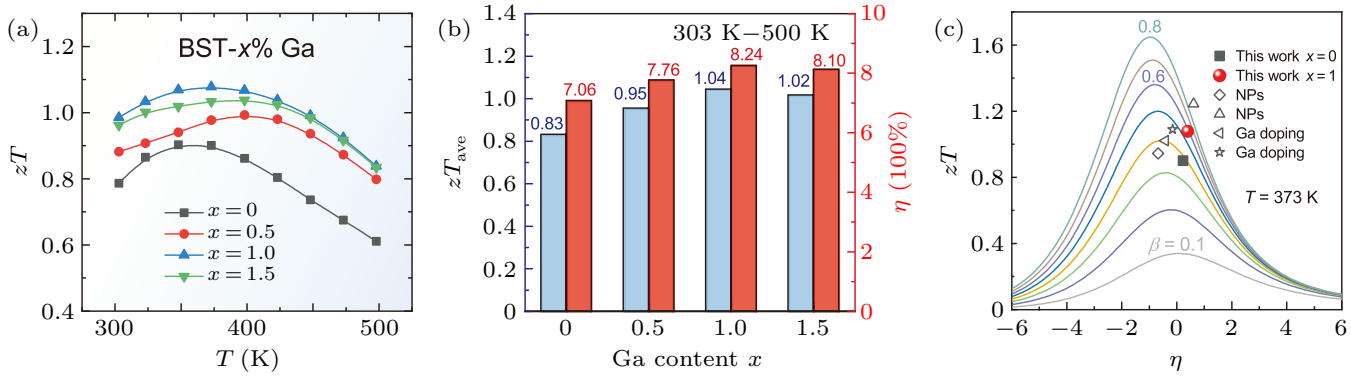


Fig. 6. (a)The zT as a function of temperature for BST-Ga samples. (b) zT_{ave} and η for BST-Ga samples in the temperature range of 303 K–500 K. (c) Experimental and predicted reduced Fermi level η dependence of zT with a different quality factor β ranging from 0.1 to 0.8. Several samples from literature data are provided for comparison.[38,48,50,51]

4. Conclusion

We successfully intercalate Ga atoms in p-type BST interlayers to improve TE properties further. Raman spectra and SEM images of BST-Ga samples reveal the origin of low κ_L, which can be attributed to multiscale phonon scattering such as point defects near the vdW interlayer, Te precipitates, and nanopores. Furthermore, the Ga intercalation enhances texture alignment to compensate for the mobility deterioration from nanopores or other defects, producing excellent $PF \sim 4.43$ mW·m^{-1}·K^{-2} in BST-Ga samples. Such synergistic effects promote a 36% increase in the quality factor β of BST-1% Ga samples in comparison to the pristine BST. Finally, a peak $zT \sim 1.1$ at 373 K is achieved in the BST-1% Ga sample and greatly improved by $\sim 22\%$ compared to the pristine BST. The defect chains induced by vdW interstitial atoms can provide valuable guidance for improving TE performance of Bi_2Te_3-based or other layered materials.

Acknowledgments

Project supported by the National Key Research and Development Program of China (Grant Nos. 2022YFB3803900 and 2018YFA0702100), the Joint Funds of the National Natural Science Foundation of China and the Chinese Academy of Sciences' Large-Scale Scientific Facility (Grant No. U1932106), and the Sichuan University Innovation Research Program of China (Grant No. 2020SCUNL112).

References

[1] Li J F, Liu W S, Zhao L D and Zhou M 2010 *NPG Asia Mater.* **2** 152
[2] Mao J, Zhu H T, Ding Z W, Liu Z H, Gamage G A, Chen G and Ren Z F 2019 *Science* **365** 495
[3] Ioffe A F, Stil'bans L S, Iordanishvili E K, Stavitskaya T S, Gelbtuch A and Vineyard G 1959 *Phys. Today* **12** 42
[4] Pei Y, Heinz N A and Snyder G J 2011 *J. Mater. Chem.* **21** 18256
[5] Chen L D, Zhang Q, Guo Z, Yan Z P, Song K, Wu G, Wang X M, Tan X J, Hu H Y, Sun P, Liu G Q and Jiang J 2021 *Mater. Today Phys.* **21** 100544
[6] Bilc D, Mahanti S D, Quarez E, Hsu K F, Pcionek R and Kanatzidis M G 2004 *Phys. Rev. Lett.* **93** 146403
[7] Heremans J P, Wiendlocha B and Chamoire A M 2012 *Energy Environ. Sci.* **5** 5510
[8] Cheng T C, Cheng C H, Huang Z Z and Liao G C 2011 *Energy* **36** 133
[9] Hsiao Y Y, Chang W C and Chen S L 2010 *Energy* **35** 1447
[10] Hsu C T, Huang G Y, Chu H S, Yu B and Yao D J 2011 *Appl. Energy* **88** 1291
[11] Fu L W, Lee K H, Kim S I, Lim J H, Choi W, Cheng Y D, Oh M W, Kim Y M and Kim S W 2021 *Acta Mater.* **215** 117058
[12] Li F, Ruan M, Jabar B, Liang C B, Chen Y X, Ao D W, Zheng Z H, Fan P and Liu W S 2021 *Nano Energy* **88** 106273
[13] Zhuang H L, Hu H H, Pei J, Su B, Li J W, Jiang Y L, Han Z R and Li J F 2022 *Energy Environ. Sci.* **15** 2039
[14] Liu H, Shi X, Xu F, Zhang L, Zhang W, Chen L, Li Q, Uher C, Day T and Snyder G J 2012 *Nat. Mater.* **11** 422
[15] He Y, Day T, Zhang T, Liu H, Shi X, Chen L and Snyder G J 2014 *Adv. Mater.* **26** 3974
[16] Zhong B, Zhang Y, Li W, Chen Z, Cui J, Li W, Xie Y, Hao Q and He Q 2014 *Appl. Phys. Lett.* **105** 123902
[17] Tao Q R, Meng F C, Zhang Z K, Cao Y, Tang Y F, Zhao J G, Su X L, Uher C and Tang X F 2021 *Mater. Today Phys.* **20** 100472
[18] Zhu B, Wang W, Cui J and He J Q 2021 *Small* **17** 2101328
[19] Liang H, Lou Q, Zhu Y K, Guo J, Wang Z Y, Gu S W, Yu W, Feng J, He J and Ge Z H 2021 *ACS Appl. Mater. Interfaces* **13** 45589
[20] Fu L, Kane C L and Mele E J 2007 *Phys. Rev. Lett.* **98** 106803
[21] Goldsmid H J 1961 *J. Appl. Phys.* **32** 2198
[22] Cheng Y D, Cojocaru M O, Keutgen J, Yu Y, Kupers M, Schumacher M, Golub P, Raty J Y, Dronskowski R and Wuttig M 2019 *Adv. Mater.* **31** 1904316
[23] Medlin D L, Yang N, Spataru C D, Hale L M and Mishin Y 2019 *Nat. Commun.* **10** 1820
[24] Callaert C, Bercx M, Lamoen D and Hadermann J 2019 *Acta Crystallogr. B* **75** 717
[25] Zhang X W, Guo Y, Zhou Z B, Li Y H, Chen Y F and Wang J L 2021 *Energy Environ. Sci.* **14** 4059
[26] Qi X, Yu Y, Xu X, Wang J C, Zhang F D, Zhu B, He J Q, Chao X L, Yang Z P and Wu D 2021 *Mater. Today Phys.* **21** 100507
[27] Wu D, Xie L, Xu X and He J Q 2019 *Adv. Funct. Mater.* **29** 1806613
[28] Lu W C, Cui W J, Zhao W, Lin W X, Liu C S, Van Tendeloo G, Sang X H, Zhao W Y and Zhang Q J 2022 *Adv. Mater. Interfaces* **9** 2102161
[29] Bludská J, Jakubec I, Drašar Č, Lošťák P and Horák J 2007 *Philos. Mag.* **87** 325
[30] Bludská J, Karamazov S, Navrátil J, Jakubec I and Horák J 2004 *Solid State Ionics* **171** 251
[31] Chen X, Li J, Shi Q, Chen Y, Gong H, Huang Y, Lin L, Ren D, Liu B and Ang R 2021 *ACS Appl. Mater. Interfaces* **13** 58781
[32] Liu W S, Zhang Q, Lan Y, Chen S, Yan X, Zhang Q, Wang H, Wang D, Chen G and Ren Z 2011 *Adv. Energy Mater.* **1** 577
[33] Sun G, Qin X, Li D, Zhang J, Ren B, Zou T, Xin H, Paschen S B and Yan X 2015 *J. Alloys Compd.* **639** 9
[34] Chen C L, Wang T H, Yu Z G, Hutabalian Y, Vankayala R K, Chen C C, Hsieh W P, Jeng H T, Wei D H and Chen Y Y 2022 *Adv. Sci.* **9** 2201353
[35] Bludska J, Jakubec I, Karamazov S, Horak J and Uher C 2010 *J. Solid State Chem.* **183** 2813
[36] Svechnikova T E, Konstantinov P P and Alekseeva G T 2000 *Inorg. Mater.* **36** 556
[37] Wang Z L, Yokoyama Y, Onda T, Adachi Y and Chen Z C 2019 *Adv. Electron. Mater.* **5** 1900079
[38] Hasan S W, Mun H, Kim S I, Cho J Y, Roh J W, Yang S, Choi S M, Lee K H and Kim S W 2013 *J. Nanomater.* **2013** 905389
[39] Zhang Z, Sharma P A, Lavernia E J and Yang N 2011 *J. Mater. Res.* **26** 475
[40] Ivanov O and Yaprintsev M 2018 *Mater. Res. Express* **5** 015905
[41] Lim Y S, Song M, Lee S, An T H, Park C and Seo W S 2016 *J. Alloys Compd.* **687** 320
[42] Gaul A, Peng Q, Singh D J, Borca T T and Ramanath G 2019 *J. Appl. Phys.* **125** 165101
[43] Richter W and Becker C R 1977 *Phys. Status Solidi B* **84** 619
[44] Souza S M, Trichês D M, de Lima J C, Grandi T A and de Biasi R S 2010 *Physica B* **405** 2807
[45] Manjon F J, Gallego P S, Rodriguez H P, Munoz A, Drasar C, Munoz S V and Oeckler O 2021 *J. Mater. Chem. C* **9** 6277
[46] Bokova M, Tverjanovich A, Benmore C J, Fontanari D, Sokolov A, Khomenko M, Kassem M, Ozheredov I and Bychkov E 2021 *ACS Appl. Mater. Interfaces* **13** 37363
[47] Yang J, Yip H L and Jen A K Y 2013 *Adv. Energy Mater.* **3** 549
[48] Zhang Y H, Xu G Y, Han F, Wang Z and Ge C C 2010 *J. Electron. Mater.* **39** 1741
[49] Zhao K, Duan H, Raghavendra N, Qiu P, Zeng Y, Zhang W, Yang J, Shi X and Chen L 2017 *Adv. Mater.* **29** 1701148
[50] Lee K H, Choi S M, Roh J W, Hwang S, Kim S I, Shin W H, Park H J, Lee J H, Kim S W and Yang D J 2015 *J. Electron. Mater.* **44** 1531
[51] Lee K H, Hwang S, Ryu B, Ahn K, Roh J, Yang D, Lee S M, Kim H and Kim S I 2013 *J. Electron. Mater.* **42** 1617